PNAS
www.pnas.org

Supplementary Information for

On the origin of the elusive first intermediate of CO_2 electroreduction

Irina V. Chernyshova[a]*, Ponisseril Somasundaran[a], and Sathish Ponnurangam[b]

[a]*Department of Earth and Environmental Engineering, Columbia University, New York, USA*
[b]*Department of Chemical and Petroleum Engineering, University of Calgary, Calgary, Canada*

*Corresponding author: irina905C@gmail.com

This PDF file includes:

www.pnas.org/cgi/doi/10.1073/pnas.1802256115

S1. Materials and Methods

S1.1. Materials, surface preparation, and conventional methods

Materials. $NaHCO_3$ (ACS certified purity >99.7%) was purchased from Sigma-Aldrich. $NaClO_4$, 98% extra pure, was from Acros. $HClO_4$ (2N aqueous) was from Ricca Chemical. $Na^{13}CO_3$ and $^{13}CO_2$, as well as D_2O were from Cambridge Isotope. Electrolyte solutions were prepared using Barnsted™ Nanopure water with a resistivity of 18.2 MΩ·cm and total organic carbon no higher than 3 ppb. All glassware was washed in a Piranha solution (1:3 H_2O_2(30%): H_2SO_4) and rinsed thoroughly with Nanopure water. Gaseous CO_2 (Lasershield grade), Ar (ultrapure), N_2 (ultrapure) and calibration gas mixtures were supplied by TechAir.

CO_2-saturated solutions were prepared by bubbling CO_2 for at least 30 min. N_2 and Ar-saturated solutions were prepared by adding salt into water that was degassed by bubbling N_2/Ar for 1 h. The salt solution was further bubbled through under stirring conditions by N_2/Ar for at least 1 h.

Electrochemical measurements. Electrolysis, cyclic voltammetry, and potentiostatic control during operando SERS were done using a Metrohm potentiostat (PGSTAT128N) controlled by NOVA 1.10.4 software. The reference electrode was an Ag/AgCl electrode (RE-5B, BASi). The counter electrode was either a Ir-Pt foil or graphite rod. *All potentials are reported in the Ag/AgCl reference scale*. The dependences on potential are additionally reported using the reversible hydrogen electrode (RHE) scale, which is calculated as

$$E(RHE)=E(Ag/AgCl)+0.209+0.059pH.$$

Surface preparation. All experiments were performed on a 0.5-mm thick copper foil (99.9985% metals basis), Alfa Aesar (catalog #11392). Its SERS active surface was prepared as follows. The foil surface was first sanded with a 400 grit SiC paper (Buehler), followed by 2-3 min ultrasonication to detach leftover abrasive particles, and rinsed with a copious amount of water. This foil was mounted into the SERS or electrochemical cell with CO_2-saturated 0.1M $NaHCO_3$, where it was subjected to 5-6 cyclic voltammetry cycles at 50 mV/s from 0 to −1.6 V (Ag/AgCl) to clean its surface further. The pre-cleaned foil was roughened by one oxidation-reduction cycle in the same electrolyte. Namely, it was polarized at +0.9 V under stirring conditions for 60 s, followed by the reduction (of the precipitated Cu oxide nanoparticles) at −0.3 V for 10 min. The cell with the mounted foil was immediately filled with a fresh Ar or CO_2-saturated electrolyte after being preliminary rinsed with the same electrolyte. A new surface was prepared before each set

of SERS measurements and each electrolysis experiment. Its reproducibility was monitored by 2-3 cycles of the 50 mV/s CVs from +0.3 to −1.3 V (Ag/AgCl) with the last cycle being in the cathodic direction from +0.3 and ending at −0.1 V.

The above SERS surface preparation protocol gives a Cu surface that has weak activity in the formate synthesis and no macroscopically detectable activity in the CO synthesis. This feature is advantageous for the purpose of our study as it allows 'cleaning up' the spectral range from peaks of adsorbed by-products including CO similar to those reported in Ref.(1), as well as to stabilize the adsorbed carboxylate.

Importantly, in agreement with others (2), we found that the copper surface is *highly susceptible to contamination by carbonaceous species from the air*, through adsorption of either atmospheric CO_2 or adventitious organics. Hence special caution was taken to minimize it.

SEM. The surface morphology was characterized using a Zeiss Sigma VP scanning electron microscope (SEM) with a Schottky thermal field emission electron gun, at a 5 kV accelerating voltage, and a 5 mm working distance.

S1.2. Operando SERS

SERS spectra were acquired using a LABRAM-ARAMIS confocal Raman microscope with a 600 grooves/mm diffraction grating. As the excitation source, a HeNe (633-nm) laser with a nominal power of 17-mW was used with or without attenuation by a filter. The monochromator was calibrated before each set of measurements using the zero order peak and the Si lattice peak at 520.7 cm^{-1} of a Si wafer reference sample.

The measurements were conducted in a one-compartment 3-electrode spectroelectro-chemical cell lab-made from a high-density polyethylene to fit a UPlanApo/IR 60X (Olympus) water-immersion objective with a working distance of 0.2 mm and the microscope stage (**Figure S1**). The objective was protected from the solution by a thin polyethylene film as described in Ref.(3). The absence of polyethylene peaks in the *in situ* spectra was verified by comparison of the spectra measured on the Cu electrode with and without the film. The microscope was focused on a relatively uniform area similar to that shown in **Figure S2**.

The spectra were measured from the open circuit potential (OCP) of ca. −0.1 V (after its stabilization) toward cathodic potentials. The cathodic limit is defined by the interference of HER because the formation of bubbles on the electrode leads to the signal loss. Electrode potential was changed step-wise each 4 min. Each spectrum was accumulated for 1 min after the 3 min allowing for the system to achieve a steady-state condition after each change of potential. During

the SERS measurements, either Ar or CO_2 was bubbled through the electrolyte, which also provided stirring of the electrolyte in the cell. The reproducibility of the spectral peaks discussed in the main text was verified with *three* duplicate experiments (**Figures S11**, **S13**, and **S15**).

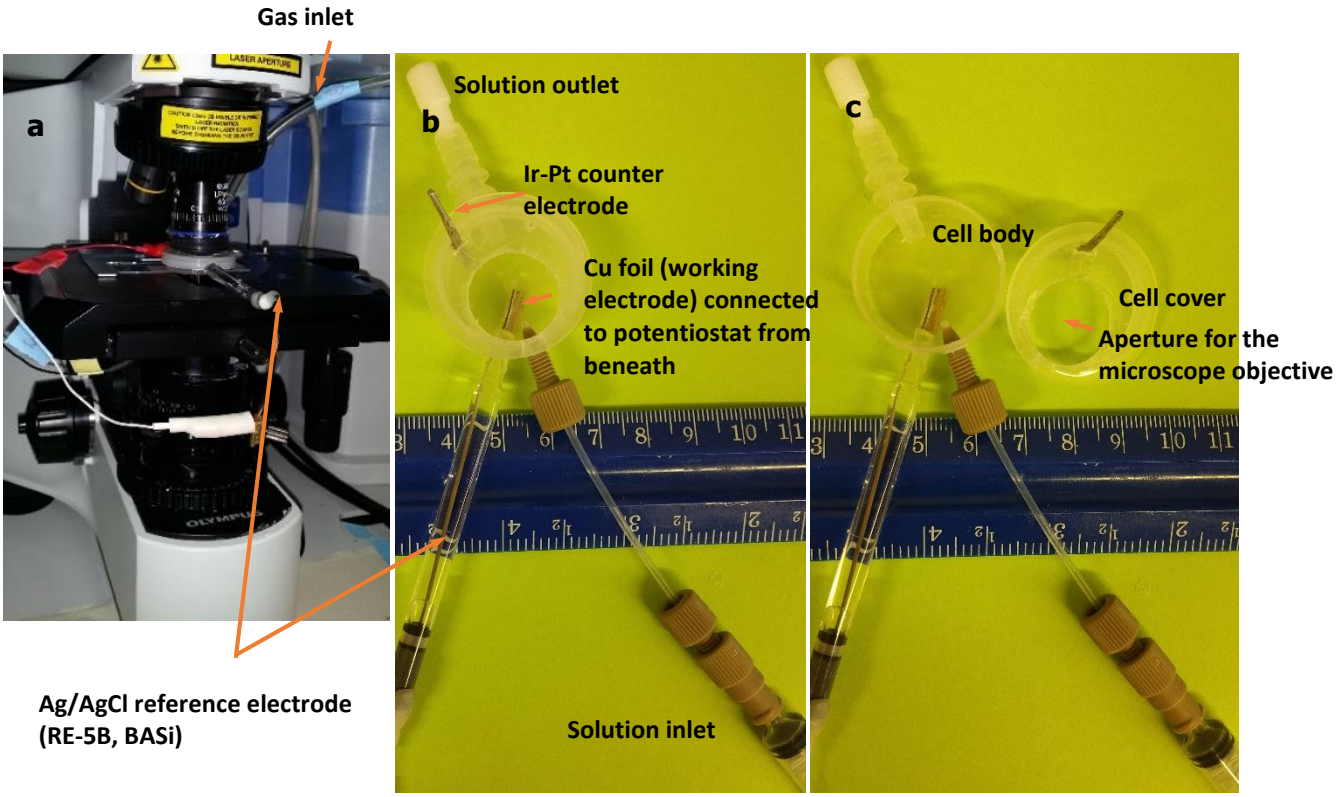

Figure S1. (**a**) The operando SERS setup based on an ARAMIS (Horiba) Raman microscope and a HDPE one-compartment spectroelectrochemical cell. (**b,c**) The spectroelectrochemical cell (4 mL) used in isotope exchange experiments. The reference electrode touches the edge of the Cu foil (working electrode) to minimize the IR drop. The cell bottom is attached to a microscope glass slide using a double-sided Scotch tape. The cell used in regular experiments is the same but, instead of the solution inlet and outlet on the cell side, it has a gas inlet and a hole in the cell cover.

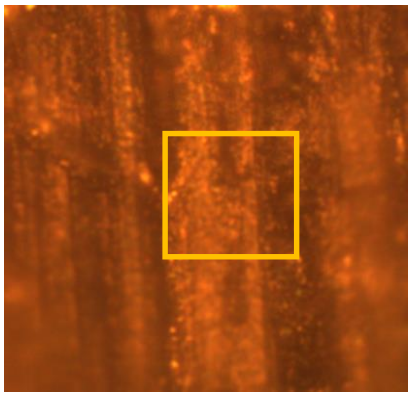

Figure S2. An optical image of a typical spot used in the operando SERS measurements. The square shows an approximate focus area of 20x20 μm^2.

To minimize errors in the H_2O/D_2O and $^{12}C/^{13}C$ isotope exchange experiments associated with the inhomogeneity of the Cu surface, the following procedure was used. The as-prepared Cu electrode was subjected to SERS measurements, without bubbling CO_2, in the lab-made flow cell shown in **Figure S1b,c.** The measurements were conducted first at OCP and then at the selected potential either in CO_2-saturated 0.05 M Na_2CO_3 or in $^{13}CO_2$-saturated 0.05 M $Na_2{}^{13}CO_3$ in D_2O. Then, without changing the microscope focus, under the applied potential, the isotope-substituted solution was continuously replaced by CO_2-saturated 0.1 M $NaHCO_3$ in H_2O and spectra were measured again.

The spectra are reported without smoothing. The peak position was determined by fitting the analyzed peaks with a Gaussian function after subtracting the baseline (**Figure S3**).

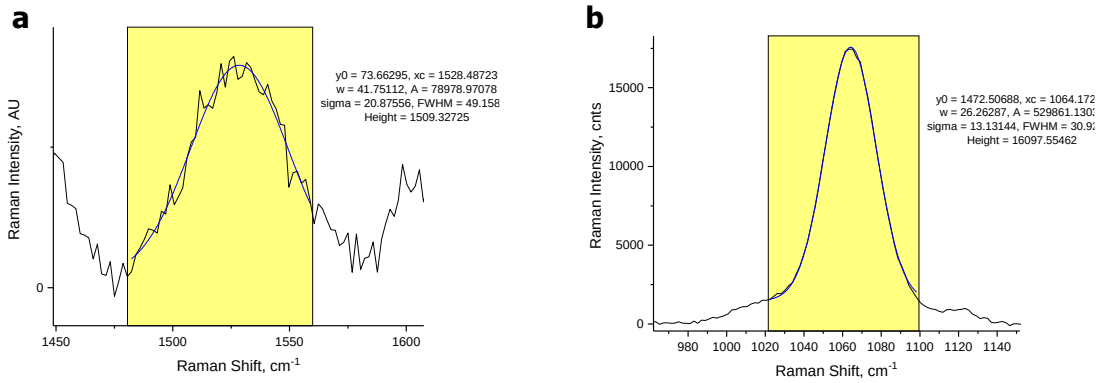

Figure S3. Examples of the peak fitting with a Gaussian function using an OriginPro 2017 gadget 'Quick fit' shown for (**a**) the $\nu_{as}CO_2^-$ peak of carboxylate and (**b**) the $\nu_1CO_3^{2-}$ peak of carbonate displayed by the spectrum measured at −0.9 V (Ag/AgCl) in **Figure S11**.

S1.3. Technical details of preparative electrolysis

Preparative electrolysis was run at constant potential on the Cu foil prepared in the same way as for the SERS experiments at potentials from −0.9 to −1.27 V using a Metrohm potentiostat (PGSTAT128N) controlled by NOVA 1.10.4 software. The experiments were performed in a modified two-compartment BASi low-volume (5 mL) electrolysis cell (MF-2040) with the compartments separated by a Nafion membrane (Nafion® 117, thickness 0.007 in., Aldrich). The reference electrode was an Ag/AgCl electrode (RE-5B, BASi). The counter electrode was either an Ir-Pt foil or graphite rod. The electrolysis conditions were: CO_2-saturated 0.1 M $NaHCO_3$ (pH 6.8), CO_2 bubbling, room temperature (295-300 K), and stirring (1500 rpm). Several additional

experiments were performed under CO_2 sealed conditions to probe gaseous products in the head space.

Since the resistivity of 0.1 M $NaHCO_3$ is as high as 130 Ω·cm, it is *critical* to take into account the iR drop in the cell. For this purpose, the uncompensated resistance R was measured using the linear i-Interrupt method of NOVA 1.10.4 software at the potential of the electrolysis twice, before and after each electrolysis experiment. The average value obtained was used to convert the applied potential to the actual one in **Figure S8**. The iR drop was found to increase with a cathodic shift of potential, which is likely to be due to the formation of H_2 bubbles on the electrode surface (4). To minimize the impact of the iR drop, the working electrode was mounted in such a way that its edge touched the reference electrode. In this configuration, the uncompensated resistance did not exceed 2 Ω and the impact of the iR on the Tafel slope at potentials less negative than −1.25 V was negligible.

Liquid products of CO_2 reduction were identified and quantified using ^{1}H NMR spectroscopy (Bruker 400SL, 400 MHz) with water suppression (an excitation sculpting pulse method). Specifically, the catholyte was diluted at a ratio of 9:1 (catholyte:D_2O) with D_2O containing 0.75 w% of trimethylsilyl propanoic acid (Sigma-Aldrich) as an internal standard. The amount of liquid products (formate) was quantified by comparing the integrated peak area of the internal standard with that of the products. The sensitivity of this method towards formate is estimated as ca. 0.5 ppm (5). Typical NMR spectra of the catholyte and amperochronometry during the electrolysis tests are shown in **Figure S4**.

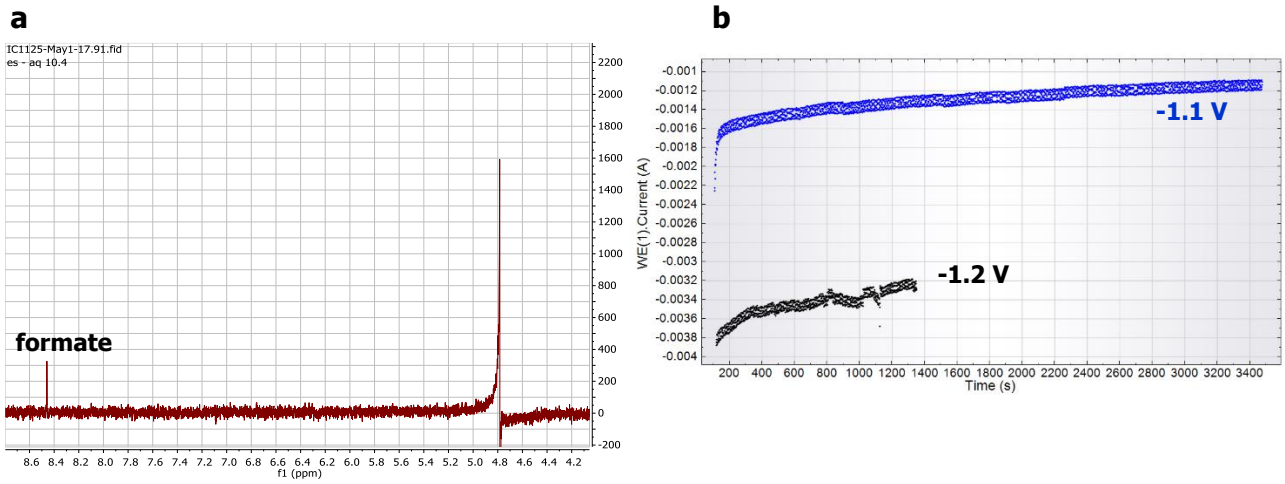

Figure S4. (**a**) A typical ^{1}H NMR spectrum of catholyte shows a formate peak at 8.45ppm. (**b**) Typical potentiostatic current curves measured during electrolysis.

Gaseous products were analyzed by injecting the sample probe into the inlet of a micro-GC (Inficon, GC 3000A) with two columns. A Molsieve column was used to separate and detect H_2, CH_4, and CO. A PLOT Q column was used for CO_2 and light hydrocarbons. For the analysis, 2.4 mL of the headspace gases was taken with a syringe through the septum and injected immediately into the micro-GC inlet in three equal portions. The results obtained with the last two portions were averaged and used for analysis. Before the measurements, the micro-GC machine was calibrated by injecting calibration gas mixtures in the same manner. The calibration gas mixtures were prepared in gas bags and equilibrated with ambient temperature and pressure for at least 1 h before the use.

Faradaic efficiency of the formate synthesis (formate selectivity) $FE_{Formate}$ is defined as

$$FE_{Formate} = N \times n \times F / Q, \qquad \textbf{[S1]}$$

where N is moles of formate synthesized, n is the number of electrons needed for this synthesis, F is the Faraday constant, and Q is the charge passed during the electrolysis.

Formate synthesis current (current selectivity) $J_{formate}$ is calculated as

$$J_{Formate} = Q \cdot FE_{Formate}/(A \cdot t), \qquad \textbf{[S2]}$$

where $FE_{Formate}$ is defined by **[S1]**, t is the electrolysis time, and A is the geometric area of the electrode.

S2. Characterization of the roughened Cu surface

SEM shows that the roughened Cu surface used in the operando SERS study is covered by 40-60-nm sintered rounded nanoparticles (**Figure S5**).

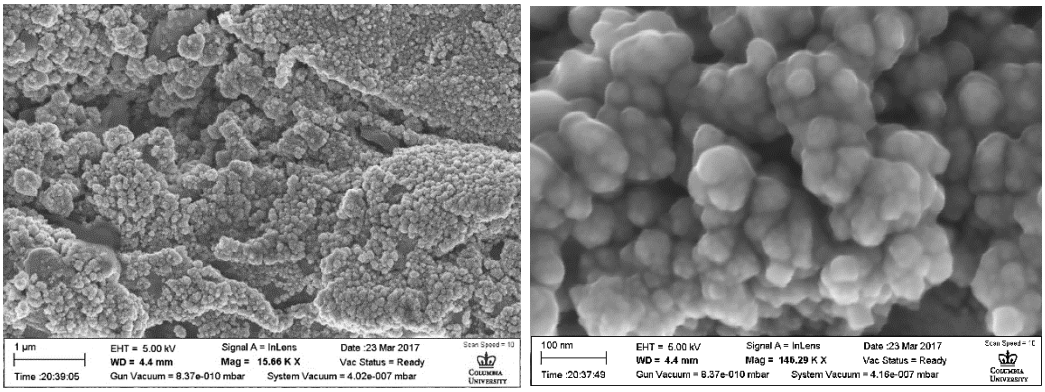

Figure S5. SEM images of the electrochemically roughened Cu surface used in operando SERS.

The roughness factor of this surface is estimated as **17±3** from the dependence of its electric double layer capacitance on the scan rate in cyclic voltammograms (CVs) (**Figure S6**) (6).

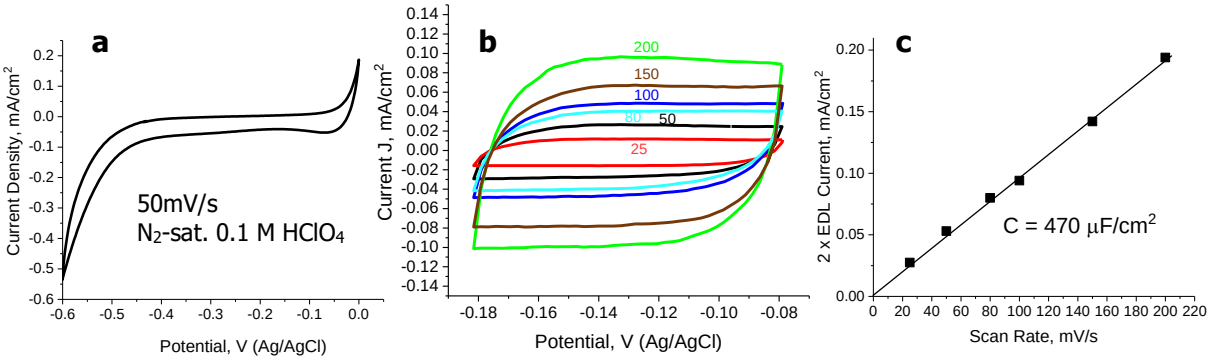

Figure S6. Assessment of surface roughness of the electrochemically roughened Cu surface in **N_2-saturated 0.1 M $HClO_4$** following the procedure of Waszczuk et al.(7) (**a**) CV is measured at 50 mV/s to indicate the ideally polarizable range of potentials, which is from -0.08 to -0.18 V (Ag/AgCl). It is similar to that reported for poly-Cu (8); (**b**) CVs measured in the ideally polarizable range at rates of 200, 150, 100, 80, 50, 25 mV/s from top to bottom; (**c**) Plot of the two-fold electric double layer (EDL) current (the width of the CVs in the vertical direction) at -0.13 V vs. scan rate gives capacitance of the Cu surface of 470 μF/cm^2 as a half of the slope. A ratio of this value to 28 μF/cm^2 assumed for a smooth surface give a surface roughness of **17 ± 3**.

The crystallographic composition of the roughened surface is assessed from the potentials of the adsorption peaks of surface hydroxyl in the CVs measured in N_2-saturated 1M KOH following Ref.(9) (**Figure S7a**). According to this technique, the surface structure is dominated by the (100), (110), and (111) crystallography. It is worth noting that the onset of the OH adsorption at ca. –0.65 V (vs. Ag/AgCl) is in perfect agreement with the thermodynamically predicted potential for this reaction on Cu (10).

The electrocatalytic activity of the roughened surface has been characterized using cyclic voltammetry (CVs) and preparative electrolysis.

Blank CVs measured in N_2-saturated 0.1 M $NaClO_4$ at pH 6.95 show two strong redox peaks—anodic at –0.23 V and cathodic at –0.52 V (Ag/AgCl) (**Figure S7b**). The formal potential of the corresponding redox process of ca. –0.37 V is below the thermodynamic potential of ca. 0.15 V of the Cu/Cu_2O couple (10). Similar underpotential redox peaks have earlier been observed on Cu in N_2-saturated acidic and basic perchlorate solutions (11-13). These peaks have been assigned to the electroformation-electroreduction of an oxygen-containing surface layer (11, 12). This assignment complies with the gradual disappearance of the Cu oxide peaks in our SERS

spectra measured in Ar-saturated 0.1 M $NaClO_4$ as the potential is scanned from –0.3 to –0.9 V (**Figure S9**). By analogy with the underpotential deposition of hydrogen on Pt group metals (14), the existence of the surface Cu oxide at potentials cathodic of the thermodynamic potential can be explained by the embedment of oxygen into the amorphous surface layer of Cu, which is promoted by the surface roughness/defects (15-17). In addition, it is predicted thermodynamically that in the potential range from –0.5 to –0.7 V hydroxyls and water are reductively desorbed which is accompanied by the adsorption of hydrogen (10). The cathodic current due to HER starts at ca. –1.0 V, at an overpotential by –200- –100 mV higher than in Refs. (11-13), indicating that our roughened Cu surface has a lower HER activity.

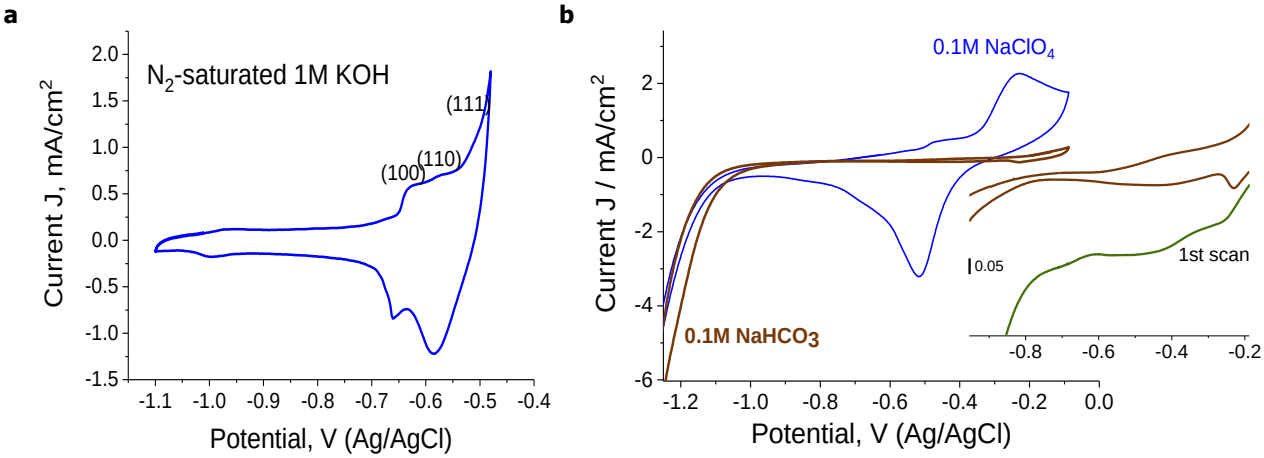

Figure S7. Cyclic voltamogramms (50 mV/s) acquired on the roughened Cu used in operando SERS (**a**) in N_2-saturated 1 M KOH (pH 13.6) to access the main surface crystallographic terminations, with the assignment of anodic peaks following Ref.(9) and (**b**) in N_2-saturated 0.1M $NaClO_4$ (pH 6.95) (thin blue line) and CO_2-saturated 0.1M $NaHCO_3$ (pH 6.8) (**thick brown line**) to identify the **onset of the electrocatalytic region at ca. –0.8 V**. The insert shows the enlarged CV measured in 0.1M $NaHCO_3$ and the first scan.

The CVs measured in CO_2-saturated 0.1M $NaHCO_3$ (**Figure S7b**) are similar in terms of the onsets of the cathodic and anodic currents to the CVs reported for Cu and Cu oxide under similar conditions (18-22). The strong peaks of the surface oxidation and reduction which are prominent in Ar-saturated 0.1M $NaClO_4$ are suppressed. This effect suggests that the CO_2/HCO_3^--derived carbonaceous adsorbates inhibit the underpotential deposition of Cu (hydr)oxide. Another notable difference is that the cathodic current is promoted as compared to the CO_2-free conditions. Its onset shifts to ca. –0.8 V and the current density increases. Given that HER dominates the reaction selectivity at low overpotentials (see below), we attribute this effect to the CO_2/HCO_3^--catalyzed HER (23). In the first scan, the onset of the cathodic current is preceded

by weak broad cathodic peaks at ca. –0.5 V and –0.7 V which may correspond to potential-induced changes in the surface composition observed in our spectra. Peaks in this potentials have earlier been reported for a Cu oxide electrode (22).

The electrolysis tests in CO_2-saturated 0.1 M $NaHCO_3$ show that in a potential range from –1.05 to –1.25 V (Ag/AgCl), that is, at overpotentials from –420 to –620 mV, the roughened Cu surface converts CO_2 to formate with the maximum Faradaic efficiency of 1.7% (**Figure S8a**). Traces of formate are also detected at –0.95 V. The co-synthesis of gaseous carbonaceous products such as CO and CH_4 is negligible in the potential range studied (no carbonaceous product is detected in the cell headspace). The dependence of the partial current density of formate synthesis J (Formate) (Eq. **[S2]**) in a semi-logarithmic scale gives a Tafel slope of 130 ± 10 mV/decade (**Figure S8b**). This value suggests that the RDS of this reaction is a Volmer-type reaction, such as reaction $CO_2 + e^- = {}^*CO_2^-$. A similar conclusion has been drawn earlier for the CO synthesis on Cu (6).

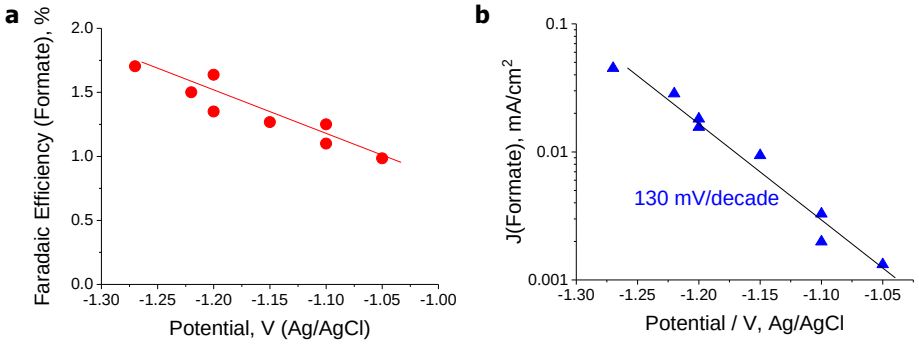

Figure S8. Catalytic activity of the roughened Cu used in operando SERS in the formate synthesis in CO_2-saturated 0.1M $NaHCO_3$ (pH 6.8): (**a**) Faradaic efficiency and (**b**) partial formate current density $J_{Formate}$. The latter gives the Tafel slope of 130 ± 10 mV/decade.

S3. Additional SERS data

S3.1. CO_2-free conditions. As a reference, we first measure operando SERS on Cu in Ar-saturated 0.1M $NaClO_4$ (**Figure S9**). These spectra are qualitatively similar to those reported earlier (1). Namely, from –0.3 to –0.7 V, they are dominated by typical peaks at ca. 415, 530, and 610 cm^{-1} of Cu(II) and Cu(I) oxides (24-27). At –0.9 V, the oxide peaks disappear, in agreement with the disappearance of the oxide reduction current in the CV (**Figure S7b**). Weak peaks at 935 and 1605 cm^{-1} are due to the electrolyte (ClO_4^- anions and H_2O molecules,

respectively). A peak at 207 cm^{-1} can be assigned to the frustrated translations of the physisorbed water (28, 29). A peak at 285 cm^{-1} is consistent with the Cu-Cl stretching vibrations of adsorbed chloride or CuCl formed by the catalytic degradation of ClO_4^- (1). We tentatively assign the remaining weak peaks at ca. 1055, 1120, 1290, 1375, 1430, and 1505 cm^{-1} to the carbonaceous species formed by electroreduction of irreversibly adsorbed CO_2 contaminations of the initial surface. The rationale for this assignment is the presence of these peaks at about ten times higher intensity under the CO_2 saturated conditions (see **Figure 2** in the main text and **Figures S11** and **S13**).

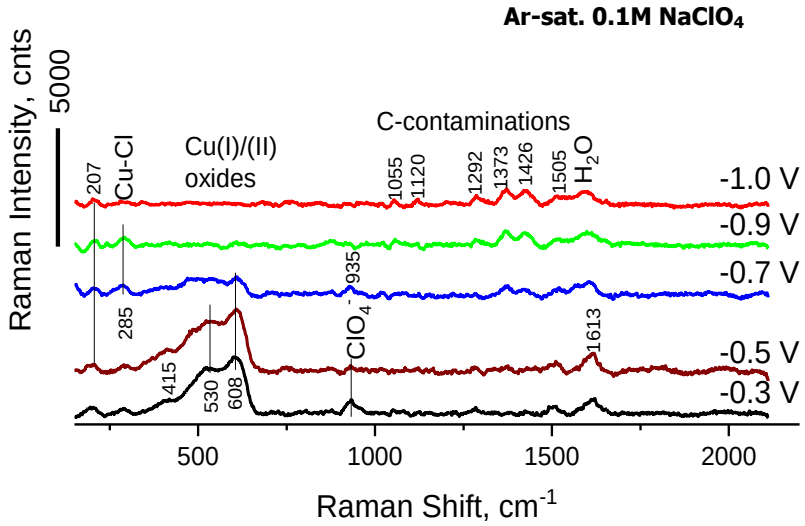

Figure S9. in situ SERS of the roughened Cu in **Ar-saturated 0.1M $NaClO_4$ (pH 6.9)**. Spectra from the open-circuit potential (OCP) of ca. –0.1 V into the cathodic direction.

S3.2. CO_2-saturated 0.1M $NaHCO_3$

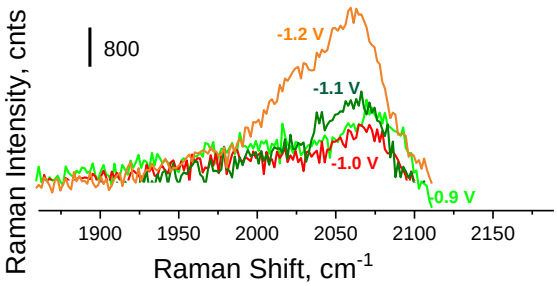

Figure S10. CO spectral region of the spectra shown in **Figure 2** in the main text shows that the νCO peak red shifts as the potential is scanned from –0.9 to –1.2 V (Ag/AgCl). The signal-to-noise ratio of this peak varies between 6 and 20.

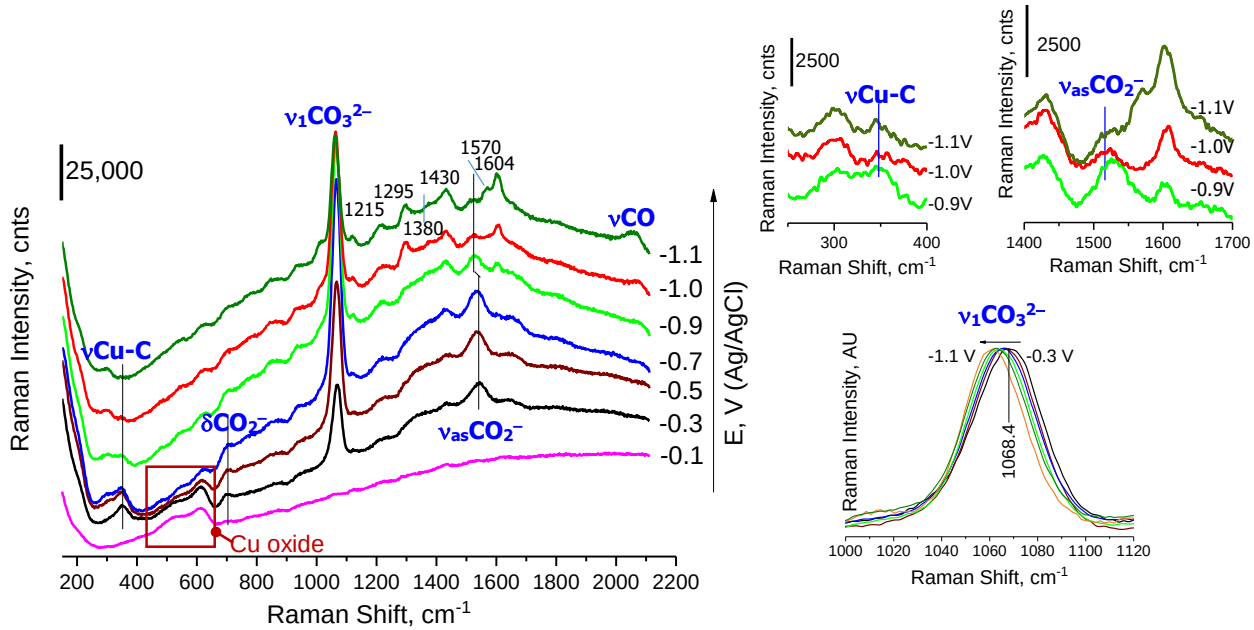

Figure S11. Operando SERS of rough Cu surface in CO_2-saturated in 0.1M $NaHCO_3$ (pH 6.8). Spectra were measured from the open-circuit potential of ca. –0.1 V toward the cathodic direction. Panels on the right show enlarged $*CO_2^-$ peaks in *the electrocatalytic region*, as well as the carbonate peak in the whole potential range.

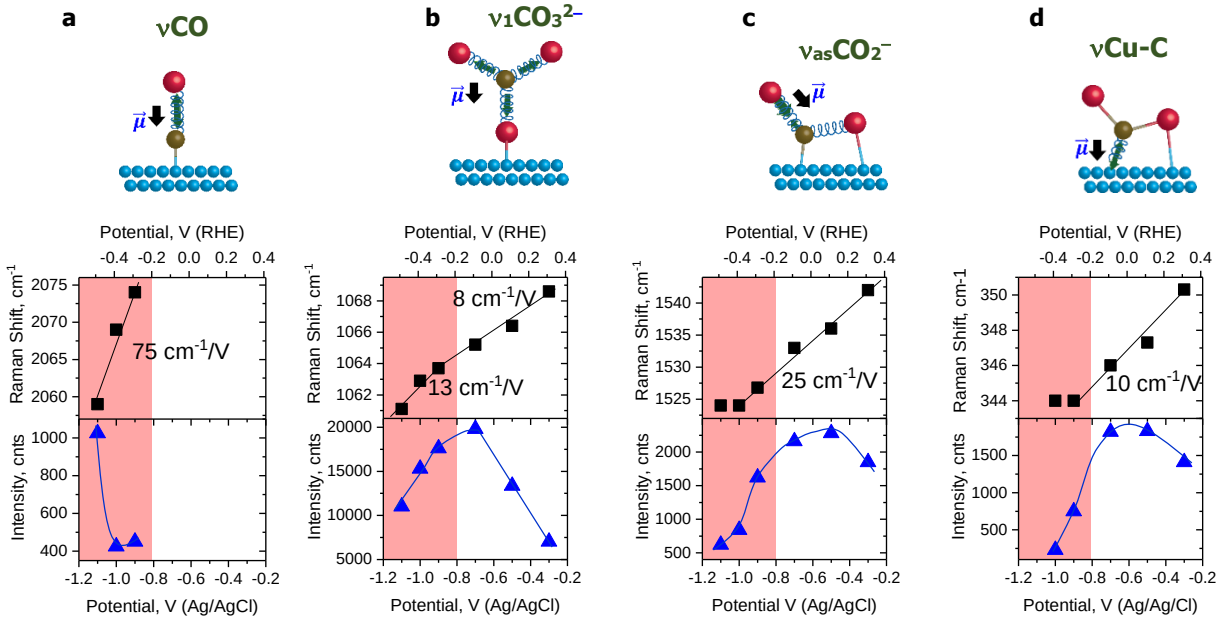

Figure S12. Effect of electrode potential on the frequencies and intensities of (**a**) νCO of adsorbed CO, (**b**) $\nu_1CO_3^{2-}$ of $*CO_3^{2-}$ and (**c**) $\nu_{as}CO_2^-$ of $*CO_2^-$ and (**d**) νCu-C of $*CO_2^-$ in the spectra shown in **Figure S11**. Black arrows in the schemes of the corresponding vibrations show the directions of their dipole moments $\vec{\mu}$. Shadowed areas show the region where cathodic current is observed (**Figure S7b**). Oxygen is red. Carbon is grey. Hydrogen is green. Copper is blue.

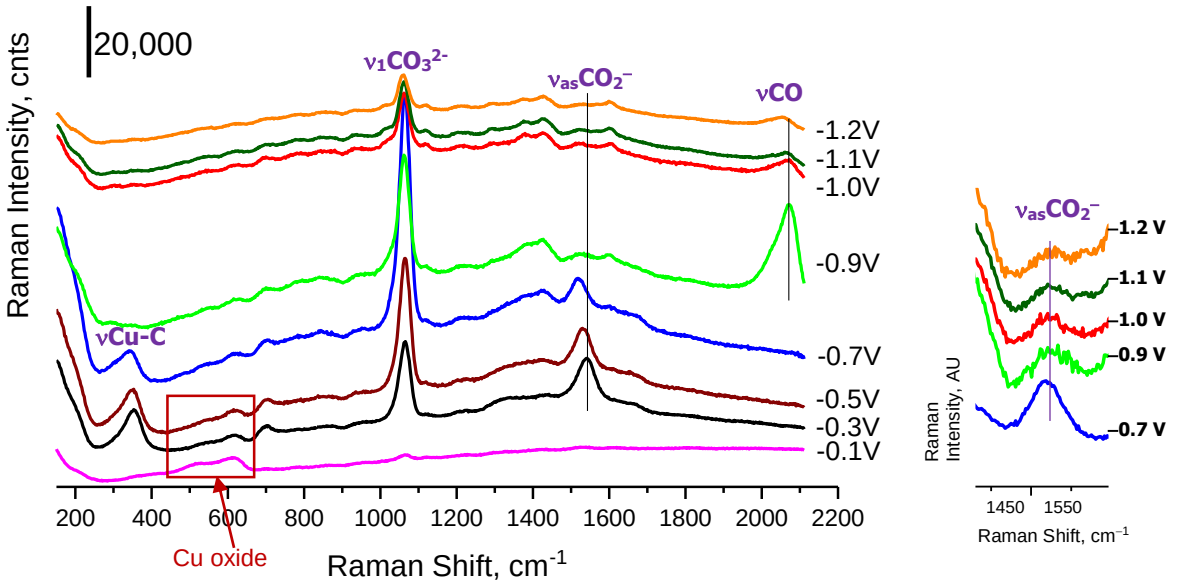

Figure S13. Operando SERS of rough Cu surface in CO_2-saturated in 0.1M $NaHCO_3$ (pH 6.8). Spectra were measured from the open-circuit potential (OCP) of ca. –0.1 V toward the cathodic direction. Panel on the right show the enlarged main $*CO_2^-$ peak in *the electrocatalytic region.*

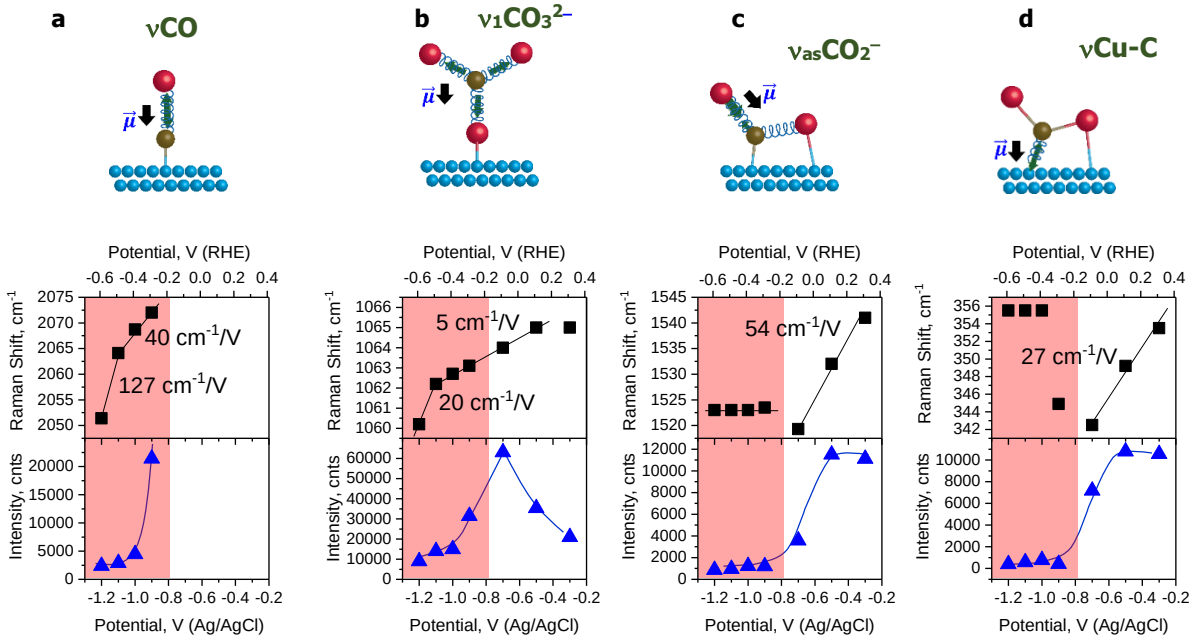

Figure S14. Effect of electrode potential on the frequencies and intensities of (**a**) νCO of adsorbed CO, (**b**) $\nu_1CO_3^{2-}$ of $*CO_3^{2-}$ and (**c**) $\nu_{as}CO_2^-$ of $*CO_2^-$ and (**d**) νCu-C of $*CO_2^-$ in the spectra shown in **Figure S13**. Shadowed areas show the region where cathodic current is observed (**Figure S7b**). Black arrows in the schemes of the corresponding vibrations show the directions of their dipole moments $\vec{\mu}$. Oxygen is red. Carbon is grey. Hydrogen is green. Copper is blue.

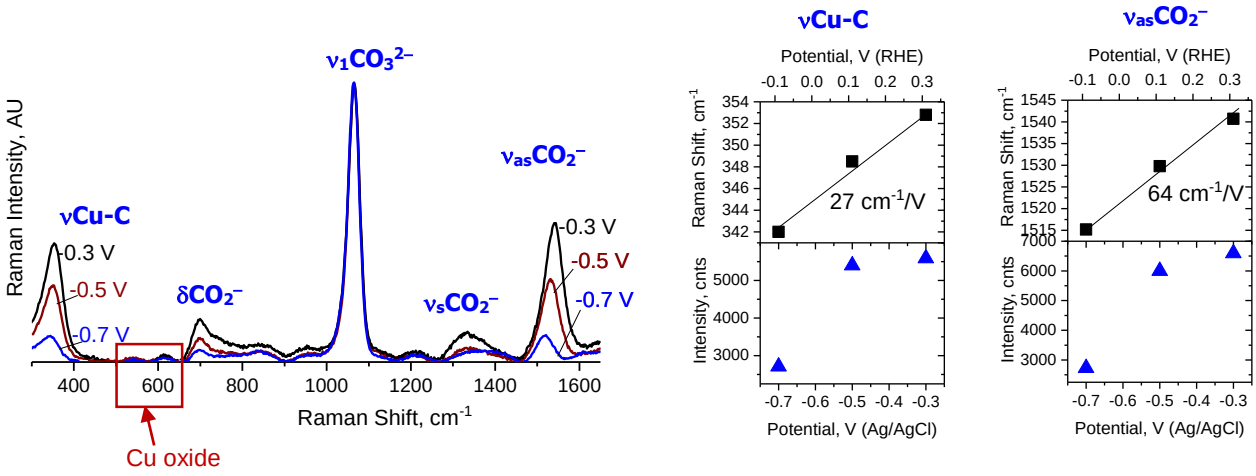

Figure S15. Operando SERS of rough Cu surface in CO_2-saturated in 0.1M $NaHCO_3$ (pH 6.8). Spectra were measured from the open-circuit potential of ca. –0.1 V toward the cathodic direction. The spectra are normalized by the intensity of the carbonate peak at ca. 1065 cm^{-1} to highlight the correlation between peaks at ca. 350, 700, 1330, and 1540 cm^{-1} assigned to $*CO_2^-$. The panels on the right show the effect of potential on the position and intensity of the νCu-C and $\nu_{as}CO_2^-$ peaks of $*CO_2^-$.

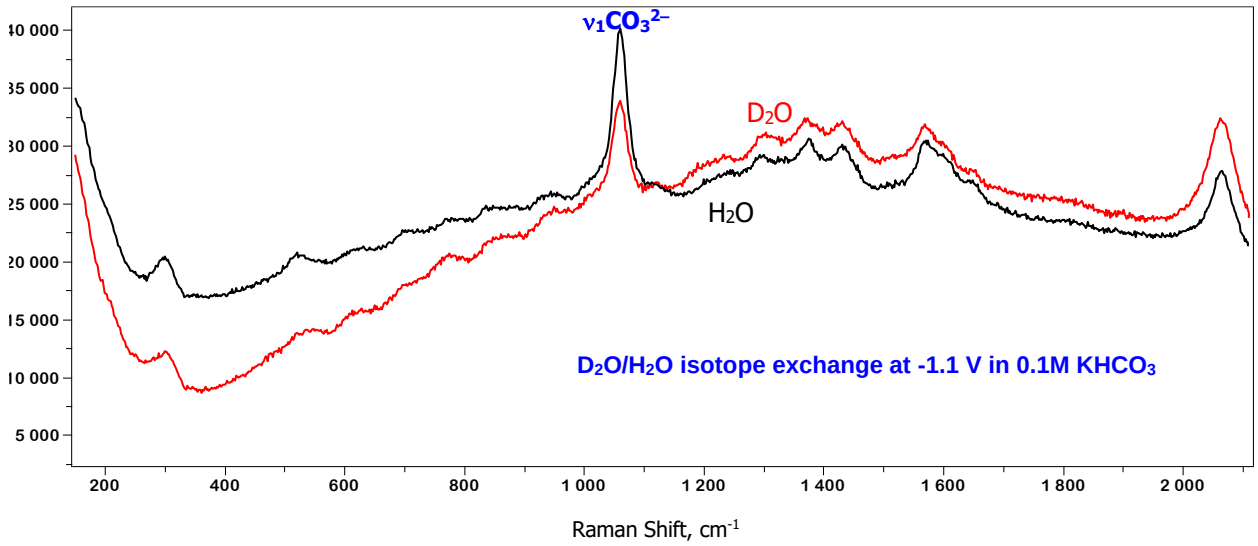

Figure S16. D_2O/H_2O isotope exchange does not have a significant impact on the SERS spectrum collected at –1.1 V (Ag/AgCl) in CO_2-saturated 0.1M $KHCO_3^-$.

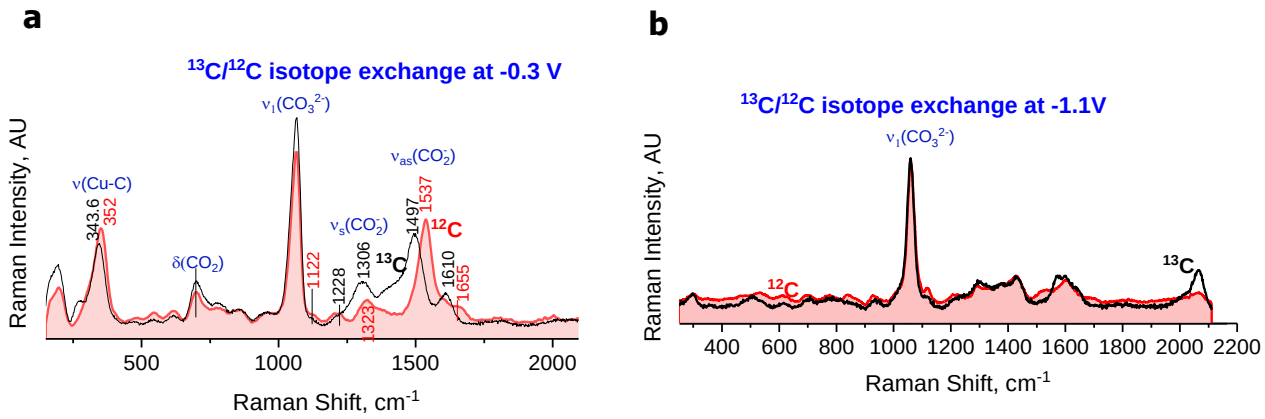

Figure S17. $^{13}C/^{12}C$ isotope exchange at (**a**) –0.3 V and (**b**) –1.1 V in $^{13}CO_2/^{12}CO_2$ saturated 0.1M $Na^{13}HCO_3$/ $NaH^{12}CO_3$ pH 6.8.

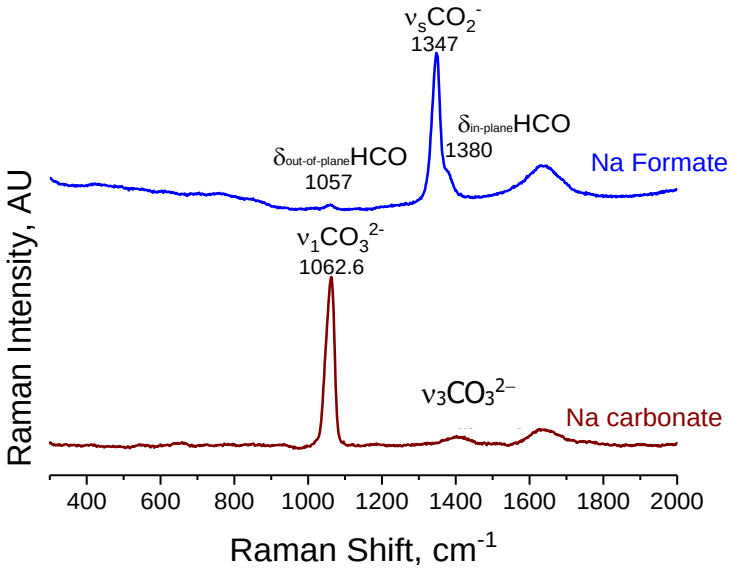

Figure S18. Raman spectra of 2M aqueous solutions of Na_2CO_3 and HCOONa measured using the same optical configuration as the SERS spectra but on mirror-level polished Pt. Peak assignment is based on Refs. (30, 31). $\nu_3CO_3^{2-}$ of CO_3^{2-} (D_{3h}) at ca. 1400 cm^{-1} is doubly degenerate, while $\nu_{as}CO_2^-$ of formate (C_{2v}) at ca. 1580 cm^{-1} is Raman silent.

S4. Incompatibility of the 1540-cm^{-1} peak with adsorbed carbonate on Cu

In this section, we first demonstrate that the earlier assignment of the 1540-cm^{-1} peak on Cu to adsorbed carbonate (19, 32-34) has not been sufficiently justified. Afterwards, we show that the 1540-cm^{-1} peak can be observed without being accompanied by the $\nu_1CO_3^{2-}$ peak at 1065-cm^{-1}, which presents clear direct evidence that the 1540-cm^{-1} peak is not due to adsorbed carbonate. Next, we confirm this result by demonstrating that the 1540-cm^{-1} peak does not correlate with the $\nu_1CO_3^{2-}$ peak at 1065-cm^{-1}. Finally, we propose that the high-frequency ν_3C-O stretching vibration of η^1-CO_3^{2-} can be associated with a poorly resolved weak peak at ca. 1430 cm^{-1}.

The earlier assignment of the peak at 1510-1540 cm^{-1} to carbonate on Cu in Refs. (19, 32-34) is based exclusively on its similar position to a peak observed on Pt(111) in CO_2 saturated perchlorate electrolytes at pH 1-3, where this peak is attributed to the ν_3C-O stretching vibration of the non-coordinated C-O bond of bidentate carbonate (adsorbed with two oxygens) (35-37). This vibration presents a high-frequency vibration that arises from coordination-induced splitting of the doubly degenerate $\nu_3CO_3^{2-}$ vibration of free CO_3^{2-} (D_{3h}) at ca. 1400 cm^{-1} (**Figure S18**). In addition, Refs. (19, 33) refer to a peak assigned to $\nu_3CO_3^{2-}$ of bidentate carbonate on Au (111) (38). However, in the latter case, the reference peak at −0.2 - −0.4 V vs. Ag/AgCl is located at ca. 1425-1450 cm^{-1} (38), which is *ca. 100 cm^{-1} lower than the peak observed on Cu under the same conditions*.

However, the earlier assignment of the 1540-cm^{-1} peak to adsorbed carbonate on a Cu electrode (19, 32-34) contradicts to the fact that carbonate formed on metallic Cu and hydrated CuO nanoparticles from gas phase is characterized by the high-frequency ν_3C-O peak at 1410-1480 cm^{-1} (39-42). Moreover, the cited studies that have assigned the 1540-cm^{-1} peak to carbonate on Pt were conducted under the conditions where *the only carbonaceous solute is CO_2* (CO_2-saturated perchlorate at pH 1-3) (35-37), *completely ignoring that Pt can activate CO_2 (43, 44)*. At the same time, the spectral region of 1500-1600 cm^{-1} is characteristic not only of the high frequency ν_3C-O stretching of bidentate carbonate, but also carboxylate (45-47), including formate (31, 40, 47, 48). Of special concern is that this peak is not accompanied by a mandatory $\nu_1CO_3^{2-}$ peak (35) which is expected in the 980-1090-cm^{-1} range (49). *Hence, the earlier assignment of the 1540-cm^{-1} peak on a roughened Cu surface in Refs. (19, 32-34) is controversial and not sufficiently justified.*

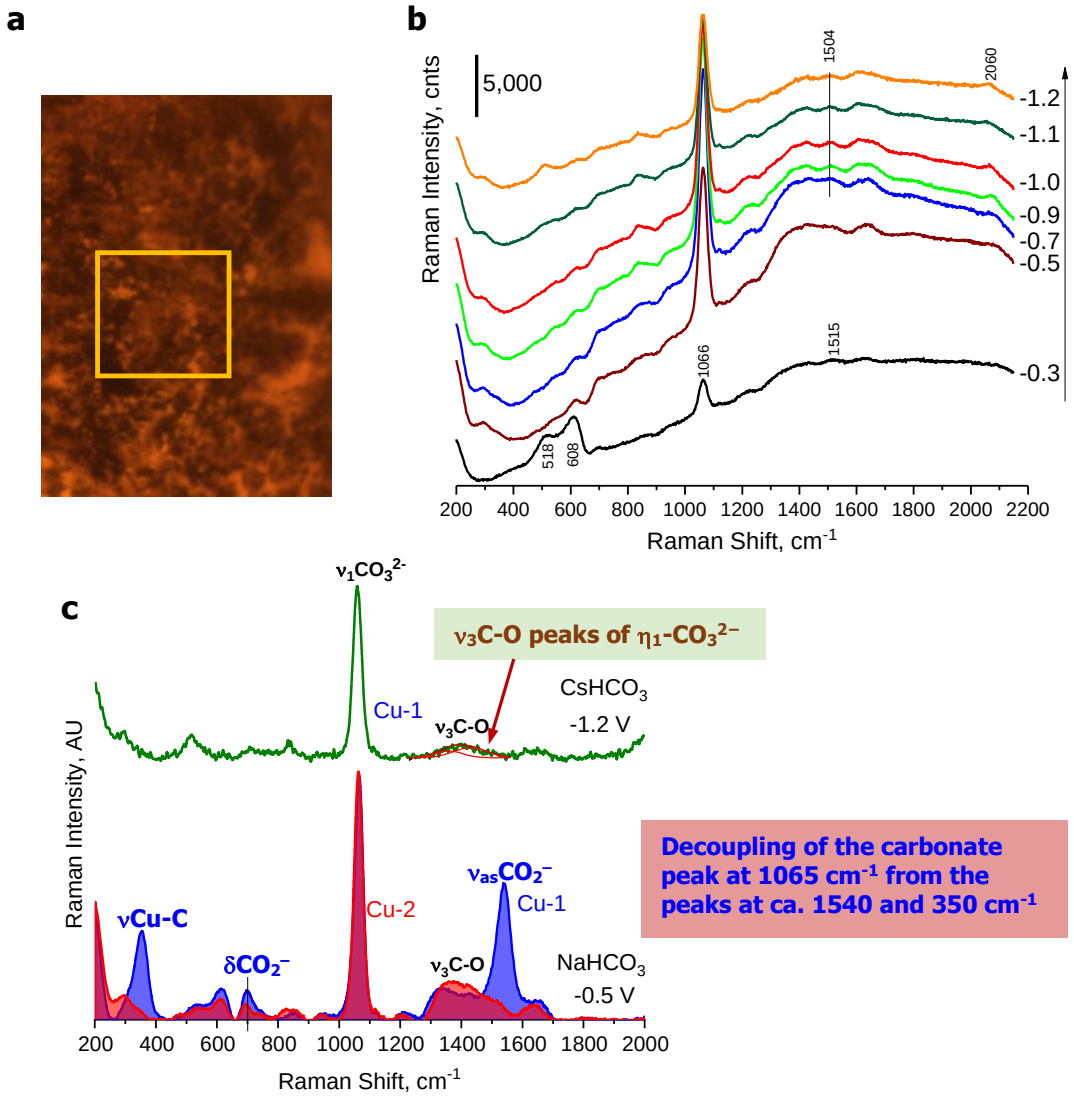

Figure S19. Decoupling of the carbonate peak $\nu_1CO_3^{2-}$ at 1065 cm^{-1} from peaks at 1540 and 350 cm^{-1} assigned to carboxylate. (**a**) Optical image of the spot (20×20 μm^2) on which the SERS spectra on Cu-2 were measured. (**b**) SERS spectra measured on Cu-2 as a function of potential starting from −0.1 V in CO_2-saturated 0.1M $NaHCO_3$. (**c**) Comparison of operando SERS measured at −0.5 V on (**red**) Cu-2 and (**blue**) Cu-1 in CO_2-saturated 0.1M $NaHCO_3$ and (**green**) a spectrum measured at −1.2 V on Cu-1 in CO_2-saturated 0.1M $CsHCO_3$. The **red** and **green** spectra do not contain the peaks at 1540 and 350 cm^{-1}, which indicates that these peaks are generated by a species different from the η^1-CO_3^{2-} carbonate characterized by the $\nu_1CO_3^{2-}$ peak at 1065 cm^{-1}. The **red** and **green** spectra also allow assignment of weak overlapped peaks at ca. 1350 and 1430 cm^{-1} to ν_3C-O of η^1-CO_3^{2-}. Cu-1 and Cu-2 label the Cu surfaces prepared by one and two consecutive oxidation-reduction cycles, respectively.

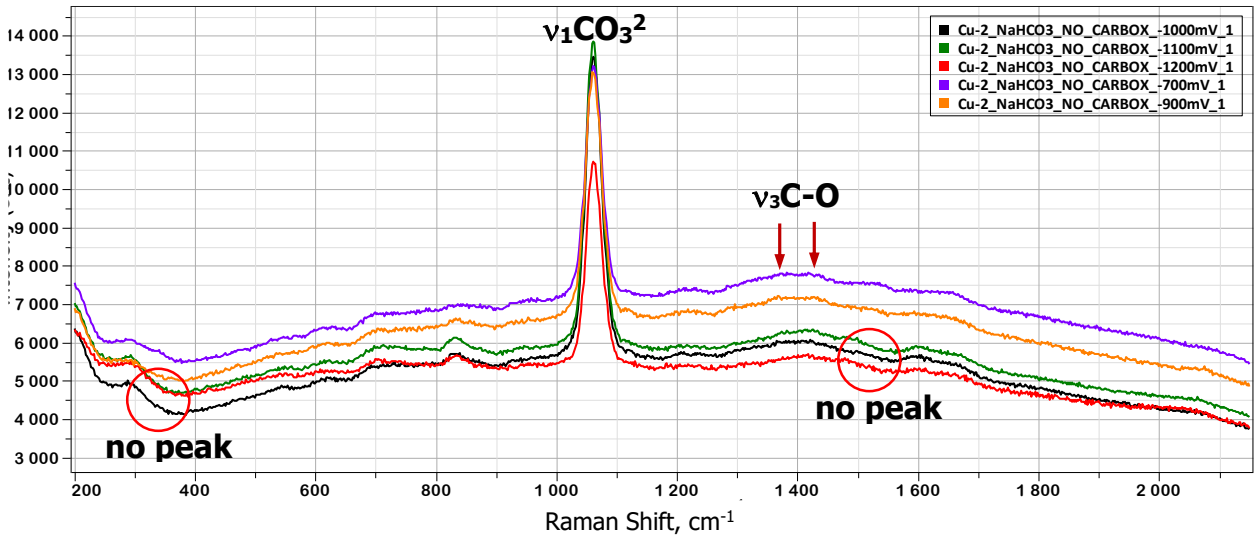

Figure S20. Duplicate SERS spectra measured on Cu-2 as a function of potential starting from −0.1 V in CO_2-saturated 0.1M $NaHCO_3$. The spectra reveal no trace of the 1540 and 350-cm^{-1} peaks while containing a strong peak of carbonate η^1-CO_3^{2-} at 1065 cm^{-1}. The absence of overlapping C-O peaks of adsorbed carboxylate allows assignment of weak poorly resolved peaks at ca. 1350-1370 and 1430 cm^{-1} to the ν_3C-O vibrations of η^1-CO_3^{2-}.

The non-carbonate origin of the 1540-cm^{-1} peak is directly demonstrated by the spectra shown in **Figures S19** and **S20**. These spectra exhibit a single carbonate peak at 1065 cm^{-1}, while the peaks at 1540 and 350 cm^{-1} (assigned to adsorbed carboxylate in the main text) are either absent or present at negligibly low intensity. These spectra were recorded on a highly heterogeneous Cu surface which was prepared by two consecutive oxidation-reduction cycles (this surface is labelled as Cu-2) (**Figure S19a**). Importantly, as seen from **Figure S19c**, the position and shape of the carbonate peak at 1065 cm^{-1} is not affected by the presence of the peaks at 1540 and 350 cm^{-1}. This excludes a possibility of the formation of two different carbonates on the Cu surface (one characterized by the $\nu_1CO_3^{2-}$peak at 1065 cm^{-1} and another characterized by the ν_3C-O peak at 1540 cm^{-1}). The peaks at 1540 and 350 cm^{-1} also selectively disappear in the electrocatalytic region (at −1.2 V) in CO_2-saturated 0.1 M $CsHCO_3$ on the Cu electrode used in the remaining experiments (labelled as Cu-1) (**Figure S19c**). The difference with the spectra recorded on Cu-1 in 0.1 M $NaHCO_3$ (**Figure 2**, **S11**, and **S13**) can be explained by the promoting role of the larger Cs^+ cation on the reaction kinetics (50), which leads to a

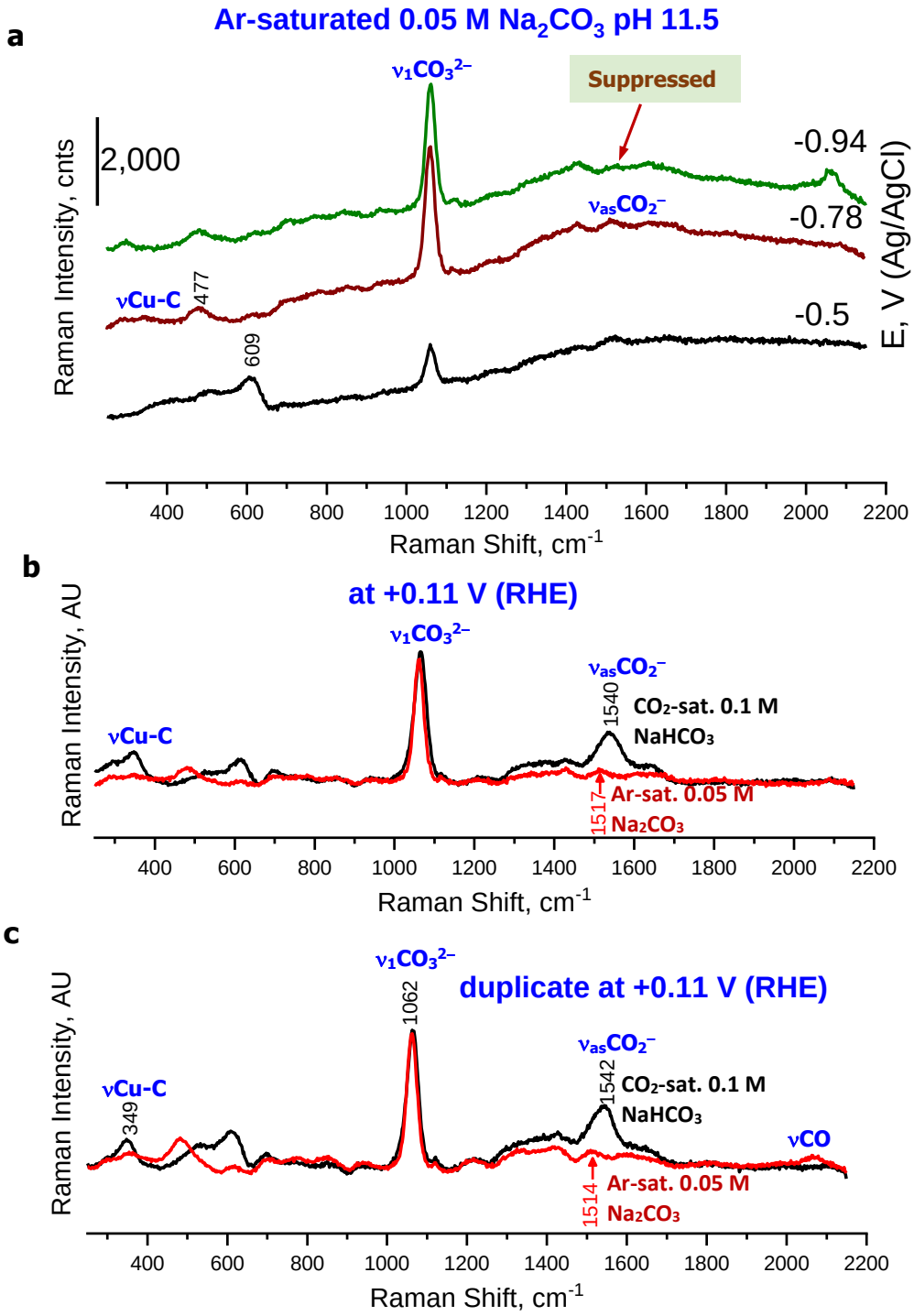

Figure S21. (**a**) Series of SERS spectra measured on Cu-1 in Ar-saturated 0.05 M Na_2CO_3 pH 11.5 starting from -0.3 V (Ag/AgCl). **(b)** SERS spectrum measured at -0.78 V (Ag/AgCl) in Ar-saturated 0.05 M Na_2CO_3 pH 11.5. For comparison, shown is the spectrum measured in CO_2-saturated 0.1 M $NaHCO_3$ pH 6.8 on the same surface at the same potential in the RHE scale before the measurements under Ar atmosphere. (**c**) Duplicates of (b) measured on a new Cu-1. To make the spectra in (b,c) comparable, they are reported at the same potential in RHE scale and normalized on the intensity of the $\nu_1CO_3^{2-}$ carbonate peak at 1062-1065 cm^{-1}.

shorter life-time of the carboxylate intermediate. The demonstrated decoupling of the carbonate peak from the peaks at 1540 and 350 cm^{-1} *indicates that the latter two peaks are not associated with adsorbed carbonate*.

The above conclusion is further strongly supported by spectra measured on the Cu-1 surface in Ar-saturated 0.05M Na_2CO_3 under bubbling Ar through the SERS cell (**Figure S21**). The preparation of the Ar-saturated solution is described in section S1.1. Under these conditions, the theoretical concentration of dissolved CO_2 is as low as **0.02 μM**, which is much lower than ca. 33 mM in the CO_2-saturated $NaHCO_3$ solution. As anticipated, the peaks at 1540 and 350 cm^{-1} *are significantly suppressed in the Ar-saturated carbonate solution as compared to the carbonate peak at 1065 cm^{-1}* (**Figure S21**). This result **confirms our assignment of the peaks at 1540 and 350 cm^{-1} to adsorbed CO_2 rather than to CO_3^{2-}** (section Carboxylate in the main text). The observed traces of the carboxylate peaks and the appearance of the peak of adsorbed CO at cathodic potentials can be explained by the exceptionally high affinity of the Cu surface to CO_2 even at such a low CO_2 concentration in the bulk solution. This result is consistent with the measurable CO_2 reduction to formate on Pd in N_2-saturated 2.8 M $KHCO_3$ at pH 9.8 (51). Moreover, it is possible that the CO_2-CO_3^{2-} equilibrium at the catalyst surface is different from that in the bulk solution (the Cu surface shifts the equilibrium to CO_2) given that CO_2 can be adsorbed as CO_3^{2-} from gas phase (15, 41).

There is also a series of other facts that are in apparent conflict with the earlier assignment of the 1540-cm^{-1} peak to bidentate carbonate. First, the most pronounced Raman peak of any carbonate is the $\nu_1CO_3^{2-}$ peak because its originates from the totally symmetric ν_1 vibration of a free carbonate anion. Therefore, the 1540-cm^{-1} peak of bidentate carbonate should be accompanied by a distinct corresponding $\nu_1CO_3^{2-}$ peak. In general, the ν_3C-O vibration of a coordinated carbonate around 1540-cm^{-1} correlates with the $\nu_1CO_3^{2-}$ peak position below 1040-1050 cm^{-1} (45, 47, 49). However, the only $\nu_1CO_3^{2-}$ peak observed is at 1065 cm^{-1}. Since this peak is close to that of free carbonate at 1063 cm^{-1}, the corresponding carbonate is adsorbed weakly, which contradicts to the assignment of the 1540-cm^{-1} peak to ν_3C-O because that would imply that the carbonate is adsorbed strongly. Hence, *it is highly unlikely that the peaks at 1540 and 1065 cm^{-1} arise from the same carbonate species*.

The above conclusion about the different genesis of the SERS peaks at 1540 and 1065 cm^{-1} is further supported by the absence of any correlation between dependences (and especially *breaks* in the dependences) of the peak positions and intensities on potential (**Figures 3**, **S12**,

S14, and **S15**). These breaks are caused by a change in the local environment or orientation of the vibrating dipole. Hence, *if the breaks observed for two vibrating dipoles are synchronized it is highly likely that these dipoles arise from the same species*. The 1540-cm^{-1} peak exhibits two breaks at ca. −0.6 and −1.0 V (**Figure 3c**), while the 1065-cm^{-1} peak has one break at −0.9 V (**Figure 3b**). *The lack of a correlation between the peaks at 1540 and 1065 cm^{-1} further supports the above conclusion that they characterize two different species.*

Finally, the $^{13}C/^{12}C$ isotope exchange effect of the 1540-cm^{-1} peak is in conflict with the high frequency ν_3C-O vibration of carbonate. In general, the $^{13}C/^{12}C$ exchange effect on the νC-O stretching vibration of carbon connected to three oxygens is stronger than that on a carbon atom connected to two oxygen atoms (52). The experiment shows the opposite relationship. The 1540-cm^{-1} peak red shifts in $^{13}CO_2$-saturated $NaH^{13}CO_3$ by a factor of 1.026±0.002 (**Figures 4a** and **S17a**). This value is similar to 1.029 and 1.027 observed for the asymmetric C-O stretching $\nu_{as}CO_2^-$ of sodium acetate (53) and $CO_2^{\bullet-}$ in the Ne matrix (54), respectively, but lower than 1.033 observed for the high frequency $\nu_3CO_3^-$ peak of HCO_3^- in water (52). Hence, $^{13}C/^{12}C$ isotope exchange effect further confirms that the 1540-cm^{-1} peak is unlikely to be the high frequency ν_3C-O vibration of carbonate.

***The aforementioned facts allow us to exclude confidently adsorbed carbonate as the possible origin of the 1540-cm^{-1} peak*.**

Finally, we attempt to locate the two ν_3C-O peaks of η^1-CO_3^{2-}. The spectra measured under the conditions where with the carboxylate peaks are suppressed (**Figure S19c, S20**, and **S21**) display weak peaks at ca. 1350 and 1430 cm^{-1} (**Figures S19c** and **S20**) or a broad peak at ca. 1350-1400 cm^{-1} which can be curve fitted with these two peaks. SEIRAS spectra measured on a Cu electrode also display a shoulder at ca. 1430-1440 cm^{-1} which has been overlooked in the SEIRAS studies (19, 33, 34). The two peaks at ca. 1350 and 1430 cm^{-1} are consistent with the ν_3C-O vibrations of η^1-CO_3^{2-}, taking into account spectra of the carbonate formed on Cu and hydrated CuO nanoparticles from gas phase (39-42) and the η^1-CO_3^{2-} carbonate formed at the Fe(III)(hydr)oxide-water interface (45, 55). The relatively weak intensity of the ν_3C-O peaks of η^1-CO_3^{2-} as compared to the $\nu_1CO_3^-$ peak can be explained by the low Raman cross-section of the $\nu_3CO_3^-$ peak of free CO_3^{2-} (**Figure S18**) combined with the weak adsorption strength of η^1-CO_3^{2-}. Strong chemisorption can enhance SERS cross-section of certain vibrations through the charge transfer mechanism (56).

S5. Comment on variations of the effect of potential on the carboxylate peaks in replicate SERS sets

The replicate sets (**Figures 2, S12, S14,** and **S15**) display variations in the dependences of the carboxylate and carbonate peaks on potential in terms of the potential values where the breaks in the dependences are observed. For example, the maximum intensity of the carbonate peak is observed at −0.9 in **Figure 3b** but at −0.7 V in **Figures S12b** and **S14b**. These variations are understandable taking into account the uncontrollable heterogeneity of the roughened Cu surface along with the small area (ca. 20x20 μm^2) probed by SERS (**Figures S2** and **S5**).

Of importance is that, despite the variations, *the spectral dependences that we use in our argument are qualitatively the same in all the sets.* Specifically, all the sets display correlation between the two carboxylate peaks at 1540 and 350 cm^{-1} and the absence of correlation between these two and the carbonate peak at 1065 cm^{-1}. The 1540 and 350-cm^{-1} have positive Stark tuning rates. The dependences of the peak positions and intensity are also qualitatively similar in all the sets. For example, the carbonate peak at 1065 cm^{-1} always experiences the Stark effect in the electrocatalytic region, while the carboxylate peaks at 1540 cm^{-1} does not.

In terms of the trends, an exception is the cancellation of the Stark effect on the carboxylate peaks at 1540 and 350 cm^{-1} at potentials from −0.3 to −0.5 V in **Figure 3c,d**, while these peaks experience the Stark effect in this potential range in **Figures S12c,d**, **S14c,d** and **S15**. The anomaly in **Figure 3c,d** can be attributed to a higher local surface density of η^2(C,O)-CO_2^- on the corresponding surface. This interpretation is based on the fact that only in **Figure 3c,d**, the peak intensities increase by a factor of 2 as potential is biased from −0.3 to −0.5 V. In contrast, the peak intensities increase only by ca. 20% in **Figure S12c,d** or are the same within the experimental error in **Figures S14c,d** and **S15**. An increase in the local surface density of vibrating dipoles is known to increase their collective vibrational frequency (57). The anomaly in **Figure 3c,d** can also be related to the higher surface coverage of the corresponding surface by Cu oxides. Hence, based on the replicates (**Figures S12c,d**, **S14c,d** and **S15**), we conclude that *the carboxylate is activated as potential is scanned from −0.3 to −0.9/−1.0 V*.

Of importance for the peak assignment is that the cancellation of the Stark effect from −0.3 to −0.5 V in **Figure 3c,d** is observed only for the two carboxylate peaks but not for the carbonate peak **Figure 3b**, which provides additional evidence that the former two belong to one species which is different from carbonate. Hence, the *exception confirms rather than conflicts our conclusion.*

S6. DFT methodology and additional data

All DFT calculations were performed using a plane wave DFT code (The Vienna Ab initio Simulation Package, VASP-5.3.3) (58-60). A spin-polarized projector augmented wave (PAW) method was used for core and valence electron treatment along with a generalized gradient approximation (GGA) exchange-correlation (XC) functional (Perdew, Burke, and Ernzerhof, PBE) (61, 62). A 3×3 supercell of Cu (111) surface was generated with three slabs of copper metal atoms and a vacuum gap of 25 Å in the direction perpendicular to the surface. The cutoff energy for the planewave basis set was fixed at 450 eV and the k-point mesh was generated using Monkhorst-Pack method (5×5×1 for surfaces). The Methfessel-Paxton scheme of order 1 was used for smearing the Fermi-level at a width of 0.1 eV. Using conjugate-gradient algorithm, the geometry of the adsorbate was relaxed while keeping the positions of the Cu atoms frozen. The optimized structures of $*CO_2^-$ were obtained by placing a Na counter ion (alone or relaxed when hydrated by 8 water molecules) *above* a relaxed linear CO_2 molecule. Errors due to self-interaction of dipoles with periodic images in the z-direction were corrected. All the slabs of Cu atoms were fixed spatially while and CO_2 and coadsorbed Na ion (with or without explicit eight water molecules) were relaxed such that the residual forces was less than 0.01 eV/Å.

The binding energy of CO_2 ΔE in the presence of hydrated Na $E_{Cu111+CO2+Na+8W}$ is calculated as

$$\Delta E = E_{Cu111+CO2+Na+8W} - E_{Cu111} - E_{CO_2} - E_{Na+8W} \text{ ,}$$

where E_{Cu111} is the DFT energy of clean Cu(111), E_{CO_2} is the energy of optimized isolated linear CO_2, and E_{Na+8W} the energy of optimized isolated sodium cation hydrated by eight water molecules. This calculation gives a binding energy of −2.16 eV.

The vibrational frequencies of CO_2 alone, $CO_2^{\bullet-}$ radical (CO_2+Na), and CO_2 with hydrated Na on Cu (CO_2+Na^++$8H_2O$) were calculated using VASP. The vibrational calculations were performed on geometry optimized structures of these systems. The vibrational calculations were performed on geometry optimized structures of these systems by displacing the carbon and oxygen atoms of CO_2 molecule, as well as of the two coordinating Cu atoms, while freezing the positions of the rest atoms. The atoms are displaced in two steps in both positive and negative directions of each of the three Cartesian dimensions with a step size of 0.015 Å. All the simulation parameters were kept the same as in the geometry optimization step with exception of the planewave basis set energy cut off and convergence criteria for the electronic self-consistent loop,

which were changed to 650 eV and 10^{-6} eV, respectively. We do not get imaginary frequencies which confirms that the optimized carboxylate structure is in a minimum energy state.

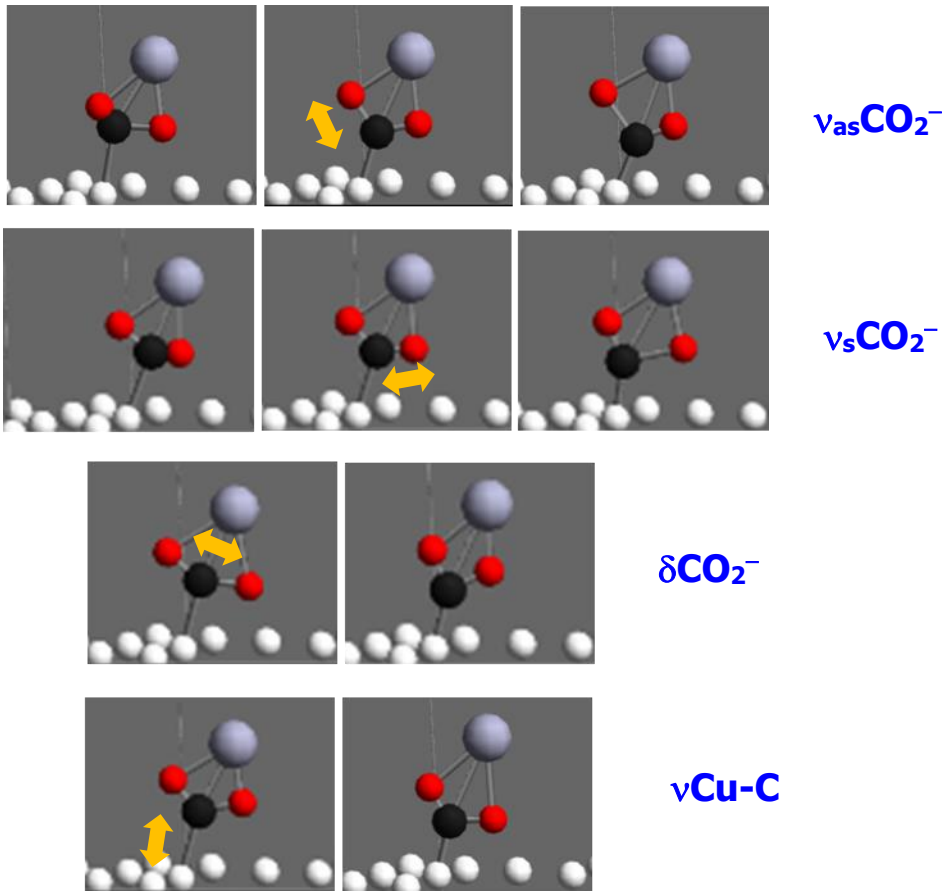

Figure S22. Vibrational forms of three main internal and one external vibrations of η^2(C,O)-CO_2^- on Cu(111) visualized using wxDragon (2.1.3). Thick bivectors show the corresponding vibrational dipoles. The η^2(C,O)-CO_2^- species is modelled as (CO_2+Na)/Cu(111). Color codes: black=C, red=O, grey=Na, small white=Cu. The forms show that $\nu_{as}CO_2^-$ presents mostly the stretching vibration of the C-O bond pointing out of the surface. $\nu_sCO_2^-$ is dominated by the stretching vibration of the C-O bond coordinated to the surface.

Table S1. Geometry, Bader charges, and binding energies of relaxed structures of free and adsorbed CO_2 on Cu(111), η^2(C,O)-CO_2^- on Cu(111) modelled as (CO_2+Na+8H_2O)/Cu(111) (**Figure 5** of the main text), as well as $CO_2^{\bullet-}$ anion radical (CO_2+Na) (**Figure 6b**).

	Free CO_2	η^2(C,O)-CO_2^-	Free $CO_2^{\bullet-}$
Bader charge (e)			
C	4.00	2.35	3.29
O1*)	-2.00	–1.85	–2.08
O2*)	–2.00	–1.62	–2.12
Total charge on CO_2	0	–1.12	–0.91
Cu11 (closest to C)	NA	0.11	NA
Cu12 (closest to O2)	NA	0.18	NA
Na^+	NA	0.99	0.98
Bond length (Å)			
C-O1	1.17	1.249	1.246
C-O2	1.17	1.357	1.246
C-Cu11	NA	1.975	NA
O2-Cu12	NA	2.060	NA
O1-Na	NA	4.012	2.268
Angle (°)			
O1-C-O2	180.0	119.1	133.9

*) O1=(free) oxygen pointing out of the surface; O2=coordinated to the surface.

Table S2. DFT-calculated vibrational frequencies of CO_2, $CO_2^{\bullet-}$ (CO_2+Na), CO_2/Cu(111), and η^2(C,O)-CO_2^- [(CO_2+Na+8H_2O)/Cu(111)]. The experimental values are in the brackets

	Free CO_2	CO_2/Cu(111)	Free $CO_2^{\bullet-}$	η^2(C,O)-CO_2^-
$\nu_{as}CO_2$	2359 (2349.1)*	2401	1702 (1658)**	1503 (1515-1525)***
$\nu_s CO_2$	1315 (1339.5)	1341	1209 (1253)	967 (1330)
δCO_2^-	632 (667.3)	580	695 (710)	733 (703)
νCu-C	-	-	-	356 (345)

*) Ref. 30;

**) In a Ne matrix. Ref. 54;

***) This work. The frequencies are shown in the electrocatalytic region where the Cu surface is negatively charged.

As seen from **Table S2**, DFT at the PBE level *predicts positions of the $\nu_{as}CO_2^-$, δCO_2^-, and νCu-C peaks of η^2(C,O)-CO_2^- well*. Their theoretical values of 1503, 733 and 356 cm^{-1} are comparable to the experimental values of 1515-1545, 703, and 345-355 cm^{-1}, respectively. There is also a good match for the frequencies of the reference systems (a free radical, free CO_2, and physisorbed CO_2). The only discrepancy we found is the significant underestimation of the frequency of the C-O stretching vibration of the surface-coordinated C-O bond of adsorbed carboxylate, $\nu_sCO_2^-$. DFT predicts its value as 960 cm^{-1}, much lower than 1330 cm^{-1} experimentally observed. This discrepancy, which does not affect our main conclusion, suggests that the DFT model we used severely underestimates vibrational modes of the groups that are strongly bound to the surface and have the vibrational dipole parallel to the surface. In fact, highly underestimated values of $\nu_sCO_2^-$ of adsorbed carboxylate are also reported by Ko et al. (63).

This discrepancy can partially be due to the strong dependence of this mode on the actual structure of the adsorption site and the DFT methodology that is employed to calculate the frequencies. In fact, DFT at the PBE level accurately predicts the C=C stretching of ethylene weakly adsorbed on Cu(111) in the horizontal geometry, with a weak dependence of this mode on the adsorption site (64). In contrast, a strong dependence of this vibration on the actual structure of the adsorption site has been shown for ethylene strongly adsorbed in a horizontal geometry on Pt (110) (it shifts from 1044 cm^{-1} for the long-bridge site to 1202 cm^{-1} for the atop site) (65). In addition, the experimental $\nu_sCO_2^-$ value of adsorbed carboxylate can be high due to its vibrational coupling with (energy transfer from (66)) a low frequency lateral translations of the carboxylate. DFT can underestimate the contributions of low frequency motions parallel to the surface (frustrated translation and rotational motions) to the entropy (67). Also, some error can be introduced by the Cartesian based displacement of atoms that we employed for frequency calculations instead of normal mode distortions (68). The C-O bond coordinated to the surface was not aligned parallel to either Cartesian X or Y directions. Hence, more detailed DFT studies are highly desirable to resolve this discrepancy.

References

1. Batista EA & Temperini MLA (2009) Spectroscopic evidences of the presence of hydrogenated species on the surface of copper during CO2 electroreduction at low cathodic potentials. *Journal of Electroanalytical Chemistry* 629(1-2):158-163.
2. Landoulsi J*, et al.* (2016) Organic adlayer on inorganic materials: XPS analysis selectivity to cope with adventitious contamination. *Applied Surface Science* 383:71-83.
3. Ren B, Wu D-Y, & Tian Z-Q (2007) Chapter 10 - In-situ Raman Spectroscopic Studies of Pyridine Adsorption on Different Transition Metal Surfaces. *In-situ Spectroscopic Studies of Adsorption at the Electrode and Electrocatalysis*, eds Sun S-G, Christensen PA, & Wieckowski A (Elsevier Science B.V., Amsterdam), pp 299-337.
4. Kapalka A, Foti G, & Comninellis C (2008) Determination of the Tafel slope for oxygen evolution on boron-doped diamond electrodes. *Electrochemistry Communications* 10(4):607-610.
5. Ponnurangam S, Yun CM, & Chernyshova IV (2016) Robust Electroreduction of CO2 at a Poly(4-vinylpyridine)–Copper Electrode. *ChemElectroChem* 3(1):74-82.
6. Li CW & Kanan MW (2012) CO2 Reduction at Low Overpotential on Cu Electrodes Resulting from the Reduction of Thick Cu2O Films. *Journal of the American Chemical Society* 134(17):7231-7234.
7. Waszczuk P, Zelenay P, & Sobkowski J (1995) Surface interaction of benzoic-acid with a copper electrode. *Electrochimica Acta* 40(11):1717-1721.
8. Lukomska A, Smolinski S, & Sobkowski J (2001) Adsorption of thiourea on monocrystalline copper electrodes. *Electrochimica Acta* 46(20-21):3111-3117.
9. Raciti D*, et al.* (2017) Low-Overpotential Electroreduction of Carbon Monoxide Using Copper Nanowires. *ACS Catalysis* 7(7):4467-4472.
10. Protopopoff E & Marcus P (2005) Potential-pH diagrams for hydroxyl and hydrogen adsorbed on a copper surface. *Electrochimica Acta* 51(3):408-417.
11. Vilche JR & Jüttner K (1987) Anion effects on the underpotential deposition of lead on Cu(111). *Electrochimica Acta* 32(11):1567-1572.
12. Gründer Y*, et al.* (2014) Cu(111) in chloride containing acidic electrolytes: Coadsorption of an oxygenated species. *Journal of Electroanalytical Chemistry* 712:74-81.
13. Tang W*, et al.* (2012) The importance of surface morphology in controlling the selectivity of polycrystalline copper for CO2 electroreduction. *Physical Chemistry Chemical Physics* 14(1):76-81.
14. Jerkiewicz G (2010) Electrochemical Hydrogen Adsorption and Absorption. Part 1: Under-potential Deposition of Hydrogen. *Electrocatalysis* (1):179–199.
15. Favaro M*, et al.* (2017) Subsurface oxide plays a critical role in CO2 activation by Cu(111) surfaces to form chemisorbed CO2, the first step in reduction of CO2. *Proceedings of the National Academy of Sciences of the United States of America* 114(26):6706-6711.
16. Eilert A*, et al.* (2017) Subsurface Oxygen in Oxide-Derived Copper Electrocatalysts for Carbon Dioxide Reduction. *Journal of Physical Chemistry Letters* 8(1):285-290.
17. Cavalca F*, et al.* (2017) Nature and Distribution of Stable Subsurface Oxygen in Copper Electrodes During Electrochemical CO2 Reduction. *The Journal of Physical Chemistry C*.
18. Hori Y*, et al.* (2005) "Deactivation of copper electrode" in electrochemical reduction of CO2. *Electrochimica Acta* 50(27):5354-5369.
19. Wuttig A*, et al.* (2016) Tracking a Common Surface-Bound Intermediate during CO2-to-Fuels Catalysis. *ACS Central Science* 2(8):522-528.

20. Baturina OA*, et al.* (2014) CO2 Electroreduction to Hydrocarbons on Carbon-Supported Cu Nanoparticles. *ACS Catalysis* 4(10):3682-3695.
21. Varela AS, Kroschel M, Reier T, & Strasser P (2016) Controlling the selectivity of CO2 electroreduction on copper: The effect of the electrolyte concentration and the importance of the local pH. *Catalysis Today* 260:8-13.
22. Wang L, Gupta K, Goodall JBM, Darr JA, & Holt KB (2017) In situ spectroscopic monitoring of CO2 reduction at copper oxide electrode. *Faraday Discussions* 197(0):517-532.
23. Costentin C, Canales JC, Haddou B, & Saveant JM (2013) Electrochemistry of Acids on Platinum. Application to the Reduction of Carbon Dioxide in the Presence of Pyridinium Ion in Water. *Journal of the American Chemical Society* 135(47):17671-17674.
24. Chan HYH, Takoudis CG, & Weaver MJ (1999) Oxide film formation and oxygen adsorption on copper in aqueous media as probed by surface-enhanced Raman spectroscopy. *Journal of Physical Chemistry B* 103(2):357-365.
25. Ren D*, et al.* (2015) Selective Electrochemical Reduction of Carbon Dioxide to Ethylene and Ethanol on Copper(I) Oxide Catalysts. *Acs Catalysis* 5(5):2814-2821.
26. Smith BD, Irish DE, Kedzierzawski P, & Augustynski J (1997) A surface enhanced Raman scattering study of the intermediate and poisoning species formed during the electrochemical reduction of CO2 on copper. *Journal of the Electrochemical Society* 144(12):4288-4296.
27. Niaura G, Gaigalas AK, & Vilker VL (1997) Surface-Enhanced Raman Spectroscopy of Phosphate Anions: Adsorption on Silver, Gold, and Copper Electrodes. *The Journal of Physical Chemistry B* 101(45):9250-9262.
28. Thiel PA & Madey TE (1987) The interaction of water with solid-surfaces - Fundamental-aspects. *Surface Science Reports* 7(6-8):211-385.
29. Galvin M & Zerulla D (2011) The Extreme Low-Frequency Raman Spectrum of Liquid Water. *Chemphyschem* 12(5):913-914.
30. Rudolph WW, Fischer D, & Irmer G (2006) Vibrational spectroscopic studies and density functional theory calculations of speciation in the CO2-water system. *Applied Spectroscopy* 60(2):130-144.
31. Rotzinger FP, Kesselman-Truttmann JM, Hug SJ, Shklover V, & Gratzel M (2004) Structure and vibrational spectrum of formate and acetate adsorbed from aqueous solution onto the TiO2 rutile (110) surface. *Journal of Physical Chemistry B* 108(16):5004-5017.
32. Oda I, Ogasawara H, & Ito M (1996) Carbon monoxide adsorption on copper and silver electrodes during carbon dioxide electroreduction studied by infrared reflection absorption spectroscopy and surface-enhanced Raman spectroscopy. *Langmuir* 12(4):1094-1097.
33. Heyes J, Dunwell M, & Xu BJ (2016) CO2 Reduction on Cu at Low Overpotentials with Surface-Enhanced in Situ Spectroscopy. *Journal of Physical Chemistry C* 120(31):17334-17341.
34. Zhu S, Jiang B, Cai W-B, & Shao M (2017) Direct Observation on Reaction Intermediates and the Role of Bicarbonate Anions in CO2 Electrochemical Reduction Reaction on Cu Surfaces. *Journal of the American Chemical Society* 139(44):15664-15667.
35. Iwasita T, Rodes A, & Pastor E (1995) Vibrational spectroscopy of carbonate adsorbed on Pt(111) and Pt(110) single-crystal electrodes. *Journal of Electroanalytical Chemistry* 383(1-2):181-189.

36. Berna A*, et al.* (2004) Structural and spectroelectrochemical study of carbonate and bicarbonate adsorbed on Pt(111) and Pd/Pt(111) electrodes. *Journal of Physical Chemistry B* 108(46):17928-17939.
37. Martinez-Hincapie R, Berna A, Rodes A, Climent V, & Feliu JM (2016) Surface Acid-Base Properties of Anion-Adsorbed Species at Pt(111) Electrode Surfaces in Contact with CO2-Containing Perchloric Acid Solutions. *Journal of Physical Chemistry C* 120(29):16191-16199.
38. Arihara K, Kitamura F, Ohsaka T, & Tokuda K (2001) Characterization of the adsorption state of carbonate ions at the Au(111) electrode surface using in situ IRAS. *Journal of Electroanalytical Chemistry* 510(1-2):128-135.
39. Akemann W & Otto A (1991) The effect of atomic scale surface disorder on bonding and activation of adsorbates: vibrational properties of CO and CO_2 on copper *Surface Science* 287/288:104-109.
40. Pohl M & Otto A (1998) Adsorption and reaction of carbon dioxide on pure and alkali-metal promoted cold-deposited copper films. *Surface Science* 406(1–3):125-137.
41. Schumacher N*, et al.* (2008) Interaction of carbon dioxide with Cu overlayers on Pt(111). *Surface Science* 602(3):702-711.
42. Gankanda A, Cwiertny DM, & Grassian VH (2016) Role of Atmospheric CO2 and H2O Adsorption on ZnO and CuO Nanoparticle Aging: Formation of New Surface Phases and the Impact on Nanoparticle Dissolution. *The Journal of Physical Chemistry C* 120(34):19195-19203.
43. Ponnurangam S, Chernyshova I, & Somasundaran P (2015) Metal Electrodes: CO_2 Reduction and Interfacial Processes. *Encyclopedia of Colloid and Surface Science*, ed Somasundaran P (CRC Press, Taylor & Francis Boca Raton), 3rd Ed Vol VI, pp 4148-4161.
44. Hori Y (2008) Electrochemical CO2 Reduction on Metal Electrodes. *Modern Aspects of Electrochemistry, Vol.2*, eds Vayenas CG, White RE, & GamboaAldeco ME), pp 89-189.
45. Chernyshova IV, Ponnurangam S, & Somasundaran P (2013) Linking interfacial chemistry of CO2 to surface structures of hydrated metal oxide nanoparticles: hematite. *Physical Chemistry Chemical Physics* 15(18):6953-6964.
46. Chernyshova IV, Ponnurangam S, & Somasundaran P (2011) Adsorption of Fatty Acids on Iron (Hydr)oxides from Aqueous Solutions. *Langmuir* 27(16):10007-10018.
47. Freund HJ & Roberts MW (1996) Surface chemistry of carbon dioxide. *Surf. Sci. Rep.* 25(8):225-273.
48. Gibson DH (1999) Carbon dioxide coordination chemistry: metal complexes and surface-bound species. What relationships? *Coordination Chemistry Reviews* 185-6:335-355.
49. Seiferth O*, et al.* (1999) IR investigations of CO_2 adsorption on chromia surfaces: Cr_2O_3(0001)/Cr(110) versus polycrystalline alpha-Cr_2O_3. *Surface Science* 421(1-2):176-190.
50. Resasco J*, et al.* (2017) Promoter Effects of Alkali Metal Cations on the Electrochemical Reduction of Carbon Dioxide. *Journal of the American Chemical Society* 139(32):11277-11287.
51. Min XQ & Kanan MW (2015) Pd-Catalyzed Electrohydrogenation of Carbon Dioxide to Formate: High Mass Activity at Low Overpotential and Identification of the Deactivation Pathway. *Journal of the American Chemical Society* 137(14):4701-4708.

52. Sheng H*, et al.* (2018) Carbon Dioxide Dimer Radical Anion as Surface Intermediate of Photoinduced CO2 Reduction at Aqueous Cu and CdSe Nanoparticle Catalysts by Rapid-Scan FT-IR Spectroscopy. *Journal of the American Chemical Society* 140(12):4363-4371.
53. Kakihana M, Kotaka M, & Okamoto M (1983) Vibrational analysis of acetate ion molecules and estimation of equilibrium-constants for their hydrogen isotopic exchange-reactions. *Journal of Physical Chemistry* 87(14):2526-2535.
54. Thompson WE & Jacox ME (1999) The vibrational spectra of CO_2^+, $(CO_2)_2^+$, CO_2^-, and $(CO_2)_2^-$ trapped in solid neon. *The Journal of Chemical Physics* 111(10):4487-4496.
55. Ponnurangam S, Chernyshova IV, & Somasundaran P (2010) Effect of Co-adsorption of Electrolyte Ions on the Stability of Inner-sphere Complexes. *Journal of Physical Chemistry C* 114(39):16517–16524.
56. Creighton JA (1986) The resonance Raman contribution to SERS - pyridine on copper or silver in aqueous-media. *Surface Science* 173(2-3):665-672.
57. Ryberg R (2007) Infrared Spectroscopy of Molecules Adsorbed on Metal Surfaces. *Advances in Chemical Physics*, (John Wiley & Sons, Inc.), pp 1-44.
58. Kresse G & Furthmüller J (1996) Efficient iterative schemes for ab initio total-energy calculations using a plane-wave basis set. *Phys. Rev. B* 54(16):11169.
59. Kresse G & Furthmüller J (1996) Efficiency of ab-initio total energy calculations for metals and semiconductors using a plane-wave basis set. *Computational Materials Science* 6(1):15-50.
60. Kresse G & Joubert D (1999) From ultrasoft pseudopotentials to the projector augmented-wave method. *Phys. Rev. B* 59(3):1758.
61. Perdew JP, Burke K, & Ernzerhof M (1996) Generalized gradient approximation made simple. *Physical Review Letters* 77(18):3865-3868.
62. Perdew JP, Burke K, & Ernzerhof M (1997) Emission in symmetric heavy ion reactions at subthreshold energies. *Phys. Rev. Lett* 78:1396-1396.
63. Ko J, Kim B-K, & Han JW (2016) Density Functional Theory Study for Catalytic Activation and Dissociation of CO2 on Bimetallic Alloy Surfaces. *The Journal of Physical Chemistry C* 120(6):3438-3447.
64. Skibbe O*, et al.* (2009) Ethene stabilization on Cu(111) by surface roughness. *Journal of Chemical Physics* 131(2):024701.
65. Bernardo C & Gomes J (2002) The adsorption of ethylene on the (110) surfaces of copper, silver and platinum: a DFT study. *Journal of Molecular Structure-Theochem* 582:159-169.
66. Tolstoy VP, Chernyshova IV, & Skryshevsky VA (2003) *Handbook of Infrared Spectroscopy of Ultrathin Films* (Wiley, Hoboken) p 710.
67. Sprowl LH, Campbell CT, & Arnadottir L (2016) Hindered translator and hindered rotor models for adsorbates: Partition functions and entropies. *The Journal of Physical Chemistry C* 120(18):9719-9731.
68. Piccini G & Sauer J (2013) Quantum chemical free energies: Structure optimization and vibrational frequencies in normal modes. *Journal of chemical theory and computation* 9(11):5038-5045.